




Defect Engineering of TIPT_2S_3 for Highly Polarization-Sensitive Photodetector

Wenyue Wang , Fangqi Liu, Jian Shi, Zixin Yang, Tongtong Wang, Bin Liu, Qiang Yu, Sicong Zhu, Xianping Wang , and Jian Wu 

Abstract—Photodetectors based on two-dimensional materials exhibit excellent performance including high specific detectivity and fast response times. However, the polarization detection performance remains to be improved. Here, we propose a strategy to improve the polarization sensitivity of TIPT_2S_3 -based photodetectors by defect engineering based on density functional theory (DFT) calculations and investigate their optoelectronic properties using quantum transport simulations at 0.2 V bias. Theoretical calculations show that the monolayer TIPT_2S_3 achieves a multifunctional output of the optoelectronic device and obtains a larger photocurrent and high extinction ratio by defect engineering under linearly polarized light irradiation. These results indicate that TIPT_2S_3 is expected to be one of the candidate materials for future optoelectronics and polarized light devices.

Index Terms—Extinction ratio, photodetectors, polarization sensitivity, TIPT_2S_3 .

I. INTRODUCTION

IN RECENT years, the polarization-sensitive photodetectors (PSPDs) has been widely used, such as remote sensing imaging, polarization sensors, thermal imaging polarimetry, and optical radar [1], [2], [3], [4]. However, conventional PSPDs usually require the additional optical filters to achieve polarization detection [5], [6], which is detrimental to the device preparation

and integration. To meet the requirements of high-performance PSPDs, including high integration, miniaturization and large extinction ratio [7], [8], [9], 2D semiconductors with anisotropy are considered as promising candidates to meet these challenges. These in-plane anisotropic 2D materials (like perovskite, black phosphorus, GeS_2 , etc.) introduce a new degree of freedom [10], [11], [12], which is of significant application for polarization detection and neuromorphic hardware [13]. However, due to low anisotropy ratio and air instability, the performance of these 2D semiconductor-based devices still do not reach the required performance for practical applications. Additionally, with the development of nanotechnology, the construction of heterojunctions and one-dimensional (1D) nanowires have been proven to be attractive approach to solve the above problem. For instance, Li et al. firstly reported that CsCu_2I_3 nanowires-based photodetector exhibit excellent polarization-sensitive photodetection in the ultraviolet range with an extinction ratio of ~ 3.16 [14], and Zhao et al. demonstrated that the p-Te/n-MoSe₂ heterojunction photodetector has a higher polarization sensitivity of 16.39 [15]. Similarly, by constructing the HgCdTe/black phosphours heterojunction, a high-performance room temperature infrared polarization-sensitive photodetector was achieved by Jiao et al. [16]. Despite this progress, there is still room for improvement in areas such as optical response and polarization sensitivity.

As a novel two-dimensional material, TIPT_2S_3 has unique optoelectronic properties which are expected to be one of the candidate materials for future optoelectronic devices. On the one hand, existing theoretical studies have demonstrated that TIPT_2S_3 has thermodynamic stability, high carrier mobility and strong visible absorption coefficient [17]. The bulk TIPT_2S_3 was synthesized experimentally in 1973 [18], and when it was exfoliated into a monolayer by mechanical peeling methods, it was converted into an indirect semiconductor with 1.60 eV [19]. On the other hand, recent investigations have suggested that defect engineering enables simple and effective modulation of the electronic structure of materials [20], [21], which greatly affects their electronic, magnetic and optical properties. Meanwhile, with technological advances in particle irradiation and plasma treatment [22], [23], the exact location of defect generation is controllable. Therefore, the optical properties of monolayer TIPT_2S_3 based on defect engineering deserve further investigation.

In this work, density functional theory (DFT) calculation was adopted to explore the modulation of the monolayer TIPT_2S_3 electronic structure through defect engineering. The results

Manuscript received 9 November 2022; revised 23 December 2022; accepted 28 December 2022. Date of publication 2 January 2023; date of current version 9 January 2023. This work was supported by the National Natural Science Foundation of China under Grant 12064017. (Corresponding author: Xianping Wang; Jian Wu.)

Wenyue Wang, Jian Shi, and Xianping Wang are with the Jiangxi Key Laboratory of Photoelectronic and Telecommunication, College of Physics and Communication Electronics, Jiangxi Normal University, Nanchang 330022, China (e-mail: ysnwuy2022@163.com; qwe2934955115@163.com; xpwang-physics@gmail.com).

Fangqi Liu, Tongtong Wang, Bin Liu, and Sicong Zhu are with the Wuhan University of Science and Technology, College of Science, Hubei Province Key Laboratory of Systems Science in Metallurgical Process, The State Key Laboratory for Refractories and Metallurgy, Wuhan 430081, China (e-mail: lfq7@wust.edu.cn; ttwang@wust.edu.cn; liubin2021@wust.edu.cn; sczhu@wust.edu.cn).

Zixin Yang and Jian Wu are with the College of Advanced Interdisciplinary Studies, National University of Defense Technology, Changsha 410073, China (e-mail: mercy_yzx@163.com; wujian15203@163.com).

Qiang Yu is with the College of Advanced Interdisciplinary Studies, National University of Defense Technology, Changsha 410073, China, and also with the Key Laboratory of Nanodevices and Applications and Key Laboratory of Nanophotonic Materials and Devices, Suzhou Institute of Nano-Tech and Nano Bionics, Chinese Academy of Sciences, Suzhou, Jiangsu 215123, China (e-mail: qyu2015@sinano.ac.cn).

This article has supplementary downloadable material available at <https://doi.org/10.1109/JPHOT.2022.3233351>, provided by the authors.

Digital Object Identifier 10.1109/JPHOT.2022.3233351

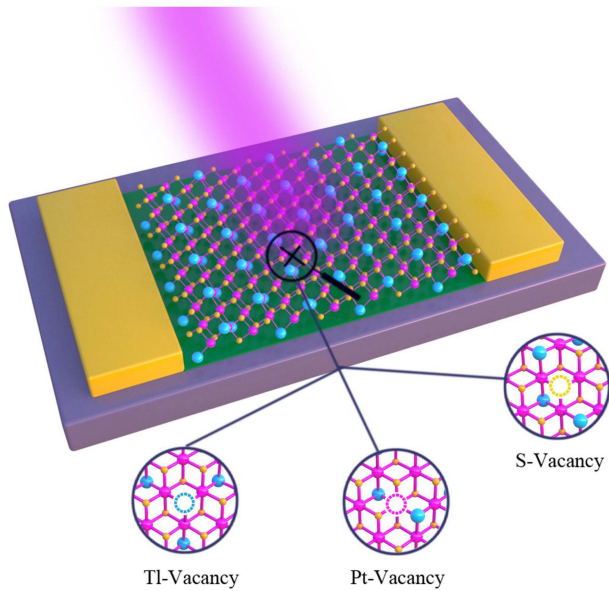


Fig. 1. Illustration of a TIPT_2S_3 photodetector irradiated by linearly polarized light.

show that the electronic structure of monolayer TIPT_2S_3 can be effectively tuned by defect engineering, especially for different Pt vacancy concentrations achieving a transformation of the all-electrical properties of TIPT_2S_3 . Further, we studied the photoelectric properties of TIPT_2S_3 monolayers based on quantum transport simulations, where DFT combined with the non-equilibrium Green's functions (NEGF) form. Calculations of extinction ratio and maximum optical response show that the devices display extremely high polarization sensitivity extinction ratio as high as 16.6 at 2.4 eV, and the defects significantly enhance the optical response and achieve special circuit system signal output.

II. MODEL AND METHODS

The calculation process of modulating the electronic structure of the pristine monolayer TIPT_2S_3 via defect engineering was completed by the Vienna Ab initio Simulation Package (VASP) [24], [25], where the specific calculation method is the Perdew-Burke-Ernzerhof (PBE) combined with generalized gradient approximation (GGA) based on the first principle. In the VASP calculation process, the electrons in the TI (4f, 5d, 6s, 6p), Pt (4f, 5d, 6s), S (3s, 3p) orbitals are used as valence electrons and the interaction between the valence electrons and the atomic real is described by the projection augmented wave (PAW) method. Furthermore, the two-probe simulation device was constructed to investigate the photocurrent of monolayer TIPT_2S_3 and its defect systems under linearly polarized light irradiation, as shown in Fig. 1. To calculate the photocurrent of these simulated devices, we adopted a theoretical method based on density functional theory combined with nonequilibrium Green's functions, and achieved by the Nanodcal package [26], [27]. Meanwhile, to obtain a continuous photocurrent, the bias of 0.2 V is exerted between the leads so that it prevents photogenerated electron-hole pairs recombination. The specific simulation

methods and calculation details are provided in Supplementary Information (see Fig. S1).

III. RESULTS AND DISCUSSION

A. Crystal Structure and Stability

First, the crystal structure of the pristine monolayer TIPT_2S_3 and the associated defect systems are optimized, as presented in Fig. S2. The plotted results indicate that there is no significant deformation in all crystal structures. Then, in order to assess the dynamic stability of the pristine monolayer TIPT_2S_3 , its phonon spectrum is evaluated on the basis of the density functional theory. Fig. S3, displays that no negative phonon frequency is entirely detected in the phonon dispersion curve of the pristine monolayer TIPT_2S_3 , indicating that the corresponding crystal structure is dynamically stable. Furthermore, the high-temperature stability of monolayer TIPT_2S_3 and the pertinent defect systems is explored by implementing molecular dynamics simulations. The variation of the total potential energy of the pristine monolayer TIPT_2S_3 and the corresponding defective system at 300-700 K is presented in Fig. S4. The aforementioned total energy oscillates slightly around a certain value for a long time without decay, and the pertinent standard deviation varies in the interval of 0–0.1, revealing the exceptional thermal stability. In addition, the average standard deviation of the potential energy is lower for 0.08 TI-vacancy and 0.08 S-vacancy (see Fig. 2(a)), indicating that proper vacancy defects are capable of enhancing high-temperature stability of monolayer TIPT_2S_3 .

B. Electronic Band Structure

To examine the influence of vacancy defects on the electronic properties of the pristine monolayer TIPT_2S_3 , the band structure of the pristine monolayer TIPT_2S_3 and the associated defect system is appropriately evaluated, as illustrated in Fig. 2(b)–(e). Besides, the achieved results corresponding to the electronic properties and band gaps are listed in Table I. These results suggest that the bandgaps of the pristine monolayer TIPT_2S_3 , 0.08 Pt-vacancy (Pt-V) and 0.08 S-vacancy (S-V) are 1.63, 0.28 and 0.45 eV, respectively. More specifically, pristine monolayer TIPT_2S_3 and 0.08 S-V systems exhibit indirect band gaps, with the conduction band minimum (CBM) and the valence band maximum (VBM located at the K-point and G-M directions, while 0.08 Pt-V system has a direct bandgap, with the CBM and VBM located at G point. The calculations demonstrate that the occurrence of vacancy defects leads to the reduction of the bandgap of pristine monolayer TIPT_2S_3 , which is similar to the example of graphene. More interestingly, for the 0.08 TI-vacancy (TI-V) system, the VBM crosses the Fermi level, which demonstrates the metal properties (see Fig. 2(e)). Then, the band structure is examined for a variety range of the Pt vacancy concentrate (see Figs. S5 and S6). The depicted results indicate that the growth of the Pt-vacancy concentration, makes the material's property transition from nonmagnetic semiconductor to magnetic metal and semiconductor. In particular, it transforms into the half-metallic material at a defective concentration of 0.04 Pt (see Fig. 2(f)). These reveal the possibility

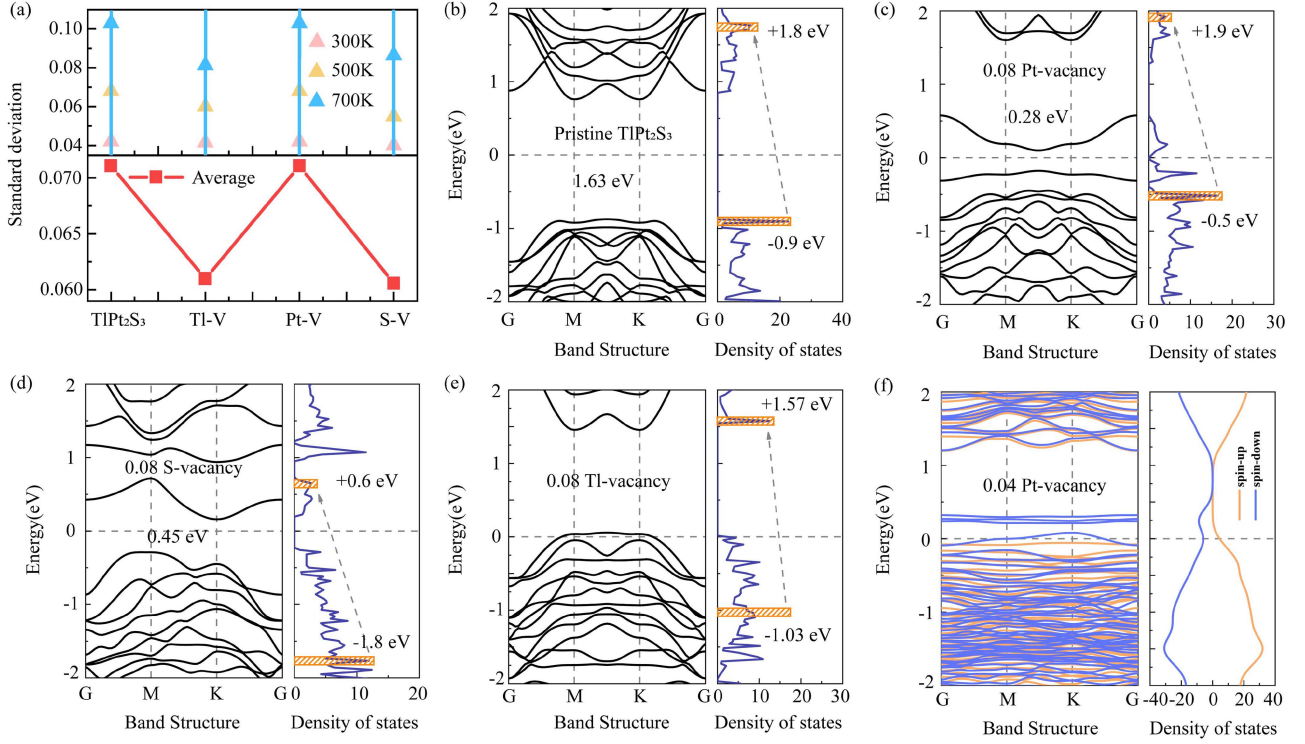


Fig. 2. (a) Standard deviation and average values of potential energy at different temperatures. (b–f) The band structure of monolayer TIPT₂S₃ and defect systems.

TABLE I
BAND GAPS, BAND TYPES AND ELECTRONIC PROPERTY AFTER STRUCTURAL OPTIMIZATION

Systems	E_g (eV)	Bandgap type	Electronic property
Pristine TIPT ₂ S ₃	1.63	Indirect	Non-magnetic semiconductor
0.08 TI-vacancy	\	\	Non-magnetic metal
0.08 Pt-vacancy	0.28	Direct	Non-magnetic semiconductor
0.08 S-vacancy	0.45	Indirect	Non-magnetic semiconductor
0.01 Pt-vacancy	1.37	Indirect	Non-magnetic semiconductor
0.02 Pt-vacancy	0.19	Direct	magnetic semiconductor
0.04 Pt-vacancy	\	\	half-metal
0.06 Pt-vacancy	0.11	Direct	magnetic semiconductor

of constructing a pristine TIPT₂S₃ monolayer with a tunable band gap and magnetic properties through defect modulation. This fact offers them a broad range of potential applications in electronics, optoelectronics and spintronics.

In order to further explain the potential physical mechanisms of defect regulation of electronic properties and magnetism, the projected density of states (PDOS) and Molecular Projected Self-Consistent Hamiltonian (MPSH) are scrutinized for all defective systems, as presented in Figs. S7–S8. The results indicate that the introduction of defects leads to the generation of defect states near the Fermi level. In some cases, the defect states cross the Fermi level to achieve the metallic transition, which enhances the electron itinerant ability of the material. For the generation of polarization, it can be seen from the MPSH that the electronic states of the pristine monolayer TIPT₂S₃ in order are concentrated around the TI and Pt atoms on the CBM and VBM. After introducing the Pt defect, the electronic states would

be mostly distributed near the S and Pt atoms on the CBM and VBM, and the distribution asymmetry leads to the generation of spin polarization. This fact is also consistent with the results of PDOS, where the VBM and CBM are mainly contributed by both the Pt-d and S-p orbitals.

C. Photoelectric Properties

In the next step, the photocurrent of the pristine monolayer TIPT₂S₃ photodetector at zero bias is evaluated, as shown in Fig. S9. The results display that the photocurrent in terms of the polarization angle (θ) qualitatively exhibits a sinusoidal shape; however, the magnitude of the photocurrent is very small and almost equal to zero. This is due to the fact that the inversion symmetry of the system has been not broken yet. As a result, to obtain a larger photocurrent, introducing an external bias voltage to break the symmetry of the system is a simple choice.

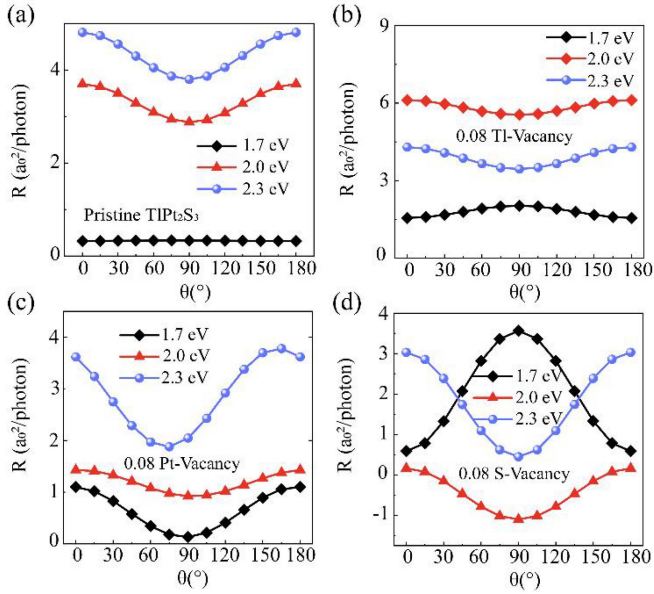


Fig. 3. The photocurrent versus polarization angle for monolayer TIPT_2S_3 and defect systems. The lines denote the fitted results.

Afterward, the photocurrents of the pristine monolayer TIPT_2S_3 and its defect systems at 0.2 V bias are studied in the photon energy interval of 1.6–2.8 eV (see Fig. S10). In Fig. 3(a)–(d), the photocurrent in terms of the polarization angle has been depicted as an example of several photon energies. These results show that the corresponding plots mostly vary in the form of $\cos(2\theta)$, which is consistent with the photogalvanic effect (PGE) phenomenological theory [28], [29]. Fascinatingly, the photocurrent of monolayer TIPT_2S_3 is almost zero at 1.7 eV (see Fig. 3(a)), which is because the photon energy is marginally greater than the band gap (i.e., 1.63 eV), making the probability of electron excitation from the VBM to the CBM is small. In addition, it is discoverable that the photocurrents of the 0.08 TI-vacancy and 0.08 Pt-vacancy systems have the same phase in the polarization angle range of 0° – 180° , while the 0.08 S-vacancy system exhibits the reverse phase. The diverse phase transition properties of these defect systems enable their potential for a variety of applications in optoelectronic devices.

The maximum photocurrent (R_{\max}) in terms of the photon energy for each system is shown in Fig. 4(a) (in which more specifically, R_{\max} represents the maximum value of the photocurrent in the range of 0° to 180° polarization angle and the photon energy could be converted to the corresponding wavelength). Evidently, in the range of simulated photon energy, R_{\max} of the 0.08 TI-vacancy system is almost always larger than that of the pristine monolayer TIPT_2S_3 system. In contrast, the maximum photocurrents of the other defect systems are smaller than the pristine monolayer TIPT_2S_3 system. These results suggest that appropriate vacancy defects are capable of enhancing the photocurrent of optoelectronic devices, and provide a promising method for improving the photoelectric response of photodetectors. This fact is essentially attributed to the vacancy defect that reduces the symmetry of the pristine monolayer TIPT_2S_3 ,

so that the electrons are unevenly distributed in the valence and conduction bands to obtain larger photocurrents.

Photoresponsivity is significant metric for evaluating photodetectors. In our simulations, the results calculated by using Nanodcal is the normalized photocurrent R , while the real photocurrent can be written as,

$$J_{ph} = R \times e \times I_\omega \times a_0^2 \times \sqrt{\frac{\mu_r}{\epsilon_r}},$$

Where the specific conversion details have been given in Section S1 of the supplementary material. We obtain a photoresponsivity of ~ 10 mA/W. Which is superior to several other 2D photodetectors on the basis of the black phosphorous [28]; nevertheless, it is much lower than the photodetectors based on the perovskite and PdTe_2 [30], [31].

Fig. 4(a) illustrates that the maximum photocurrent of each system exhibits multiple peaks in the photon energy range. For instance, the pristine monolayer TIPT_2S_3 photodetector takes its maximum photoresponse (PR) peak at 2.7 eV, while the maximum PR peak of the 0.08 TI-vacancy system takes place at 2.6 eV. In addition, the peak of maximum PR is located at 2.4 eV for the 0.08 Pt-vacancy and 0.08 S-vacancy systems. To explain the reason for the generation of PR peaks, the density of states (DOS) is calculated for each defect system, as presented in Fig. 2(b)–(e). These plots assist us in effectively realizing the process of electron transition. As shown in Fig. 2(b), for the pristine monolayer TIPT_2S_3 system, there exists a significant DOS peak located at -0.9 eV in the valence band portion, and another significantly DOS peak observed located at 1.8 eV in the conduction band portion (the peaks have been marked by the orange-colored rectangles). According to Fermi's golden rule, the probability of electron transitions between these two peaks is proportional to the density of the state's peak, which results in a photocurrent peak by absorption of 2.7 eV of photon energy. Similarly, for other defect systems, there is a larger probability of electron transition at the maximum photocurrent peak.

The polarization sensitivity is vital parameter in measuring the polarization performance of the photodetector. Since the photocurrent of each defect system demonstrates a trend similar to the function $\cos(2\theta)$ about the polarization angle, which makes possible the polarization detection [28], [32]. We introduce an extinction ratio (ER) to describe the sensitivity, which is defined as R_{\parallel}/R_{\perp} or R_{\perp}/R_{\parallel} . Here, R_{\parallel} and R_{\perp} stands for the photocurrents at the polarization angles of 0° and 90° , respectively. The variation of the ER versus photon energy for each system is presented in Fig. 4(b). The results display that for the monolayer TIPT_2S_3 photodetector, the corresponding ER fluctuates as a function of the photon energy around 1. This is because the pristine monolayer TIPT_2S_3 is an isotropic material. It is also worth mentioning that the 0.08S-vacancy has an extinction ratio of up to 16.6 at 2.4 eV, which is superior to other photodetectors. For example, the extinction ratio of the photodetector of the black phosphorus is 8.7 [3], while the experimentally measured ER of the PbS photodetector is 2.38 [33]. These results indicate that proper vacancy defects are capable of enhancing the polarization sensitivity of optoelectronic devices.

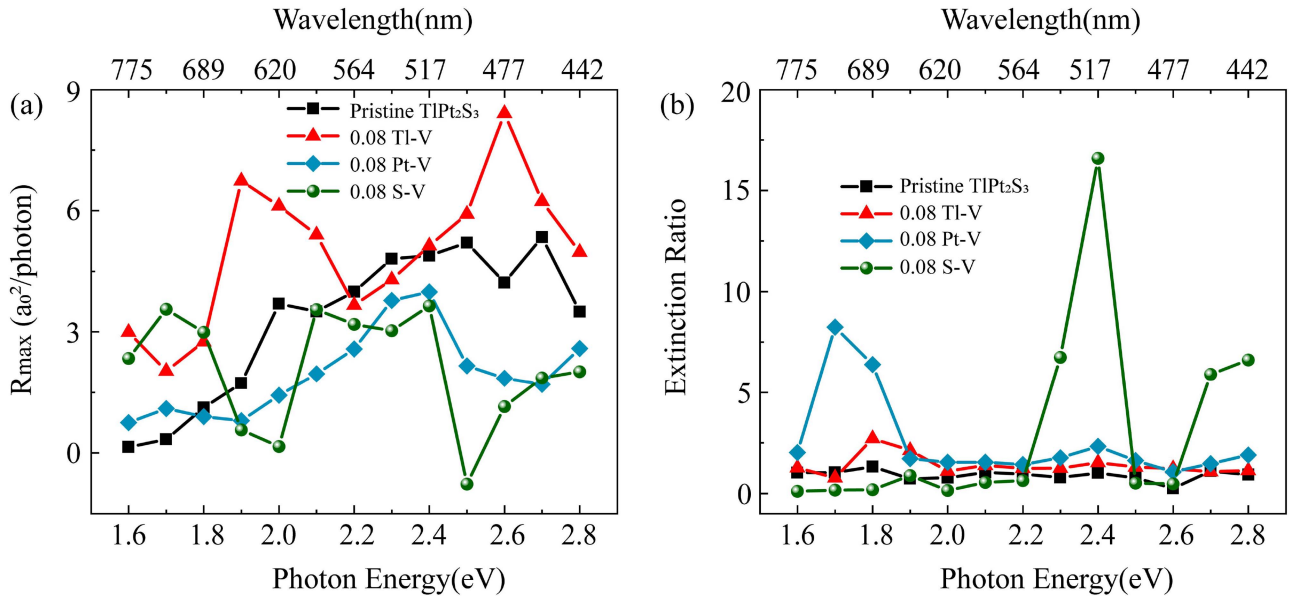


Fig. 4. (a) The variation of the maximum photocurrent with the photon energy for the monolayer TIPT_2S_3 and defect systems. (b) The extinction ratio of the photocurrent for the monolayer TIPT_2S_3 and defect systems.

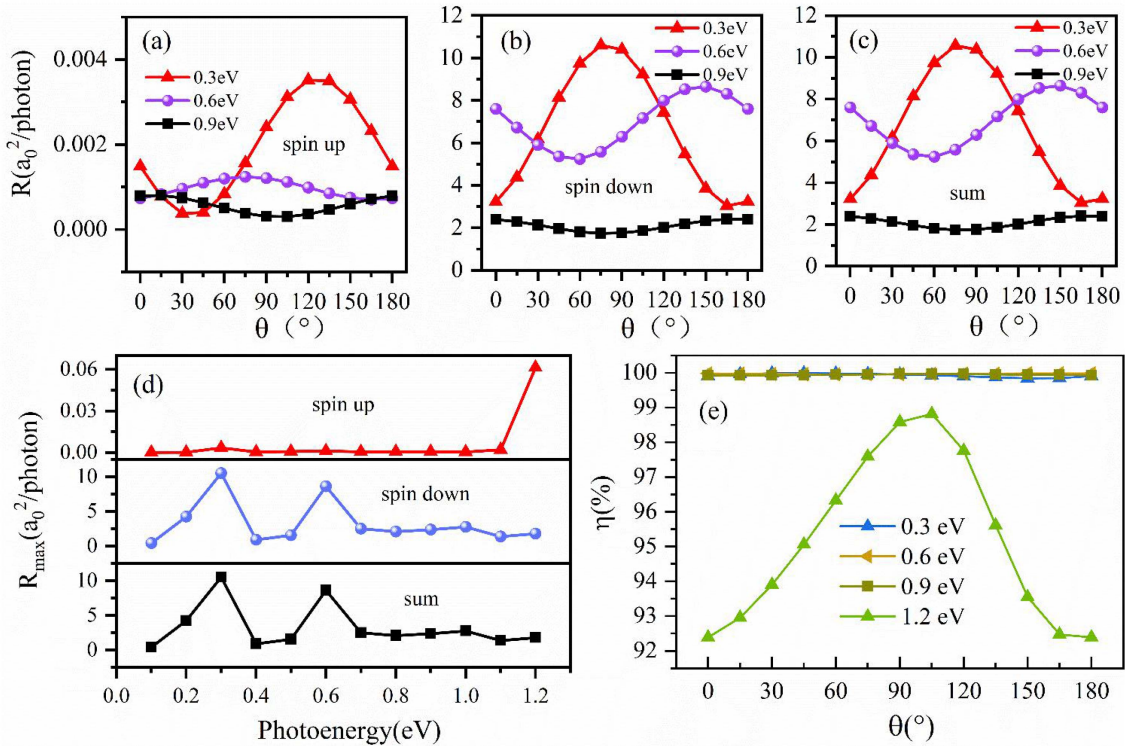


Fig. 5. 0.04 Pt-vacancy photodetector with a bias of 0.2 V between the two electrodes. (a–c) Photocurrent versus polarization angle θ . (d) Maximum photocurrent versus photon energy. (e) SET as a function of polarization angle θ .

As mentioned earlier, we further investigated whether the 0.04 Pt vacancy is employed as a candidate material for future spin photodetector devices. The variation of photocurrent is still similar to function $\cos(2\theta)$, with the polarization angle of θ (see Figs. 5 and S11). The results in Fig. 5(a)–(c) reveal that the photocurrent in terms of polarization angle for three levels of

the photon energy (i.e., 0.3 eV, 0.6 eV, and 0.9 eV). It can be also found that the spin-down current is almost the same as the total current, while the spin-up current is very trivial and nearly zero. The maximum photoelectric response of Fig. 5(d) shows that TIPT_2S_3 with this system achieves a special triangular wave circuit signal, while also filtering to obtain a spin-down current.

The spin-injection efficiency (SIE) measures the degree of spin polarization in the transport current, and the SIE is defined as $\eta = \frac{|I_{\uparrow} - I_{\downarrow}|}{|I_{\uparrow} + I_{\downarrow}|}$. Therefore, the SIE of the spin current is plotted at a bias of 0.2 V (see Fig. 5(e)). It can be observed that near-perfect spin filtering effect and the full spin-polarized photocurrent (FSPC) can be obtained at full photon energy. These results indicate that the concentration of defects could also modulate the electronic structure of the material, which potentially provides it for a diverse range of applications in spintronic devices.

IV. CONCLUSION

In summary, the modulation of the electronic structure of pristine monolayers of TiPt_2S_3 by defect engineering was investigated both from the perspective of different atoms types and concentrations of defects. Different atoms types of defects achieved a tunable band gap in the material, while further variations in the concentration of Pt atomic defects introduced magnetic properties. In addition, the obtained results from the molecular dynamics simulations revealed that the defective system exhibits better high temperature stability than that of the pristine TiPt_2S_3 . The quantum transport simulations based on TiPt_2S_3 optoelectronic devices also showed an extremely high polarization sensitivity of 16.6, with significant enhancement of photoelectric response, and realization of 100% spin filtering effect. We demonstrated that defect engineering could achieve high polarization sensitivity and strong photoelectric response output of TiPt_2S_3 -based optoelectronic devices. This issue effectively suggests that defect engineering could be implemented as an effective strategy to enhance the optoelectronic performance of photoelectric detectors in the future.

REFERENCES

- [1] Z. Li et al., "Broadband GaAsSb nanowire array photodetectors for filter-free multispectral imaging," *Nano Lett.*, vol. 21, no. 17, pp. 7388–7395, 2021.
- [2] J. Xiong et al., "High performance self-driven polarization-sensitive photodetectors based on GeAs/InSe heterojunction," *Adv. Opt. Mater.*, vol. 9, no. 20, 2021, Art. no. 2101017.
- [3] P. K. Venuthurumilli et al., "Plasmonic resonance enhanced polarization-sensitive photodetection by black phosphorus in near infrared," *ACS Nano*, vol. 12, no. 5, pp. 4861–4867, 2018.
- [4] Y. Liu et al., "Intrinsic strong linear dichroism of multilayered 2D hybrid perovskite crystals toward highly polarized-sensitive photodetection," *Adv. Opt. Mater.*, vol. 7, no. 23, 2019, Art. no. 1901049.
- [5] Y. Yu et al., "Tunable alloying improved wide spectrum UV-vis-NIR and polarization-sensitive photodetector based on SB-S-Se nanowires," *IEEE Trans. Electron Devices*, vol. 68, no. 8, pp. 3887–3893, Aug. 2021.
- [6] Z. Guo et al., "High-performance polarization-sensitive photodetectors on two-dimensional β -InSe," *Nat. Sci. Rev.*, vol. 9, no. 5, 2022, Art. no. nwab098.
- [7] R. Maiti et al., "Strain-engineered high-responsivity MoTe_2 photodetector for silicon photonic integrated circuits," *Nature Photon.*, vol. 14, no. 9, pp. 578–584, 2020.
- [8] P. Li and Z. Zhang, "Self-powered 2D material-based pH sensor and photodetector driven by monolayer MoSe_2 piezoelectric nanogenerator," *ACS Appl. Mater. Interfaces*, vol. 12, no. 52, pp. 58132–58139, 2020.
- [9] Y. W. Zhou et al., "High extinction ratio super pixel for long wavelength infrared polarization imaging detection based on plasmonic microcavity quantum well infrared photodetectors," *Sci. Rep.*, vol. 8, no. 1, 2018, Art. no. 15070.
- [10] Y. Yang et al., "Polarization-sensitive ultraviolet photodetection of anisotropic 2D GeS_2 ," *Adv. Funct. Mater.*, vol. 29, no. 16, 2019, Art. no. 1900411.
- [11] L. Ye et al., "Highly polarization sensitive infrared photodetector based on black phosphorus-on- WSe_2 photogate vertical heterostructure," *Nano Energy*, vol. 37, pp. 53–60, 2017.
- [12] Y. Ping et al., "Polarization sensitive solar-blind ultraviolet photodetectors based on ultrawide bandgap KNb_3O_8 nanobelt with fringe-like atomic lattice," *Adv. Funct. Mater.*, vol. 32, no. 24, 2022, Art. no. 2111673.
- [13] L. Tong et al., "2D materials-based homogeneous transistor-memory architecture for neuromorphic hardware," *Science*, vol. 373, no. 6561, pp. 1353–1358, 2021.
- [14] Y. Li et al., "Solution-processed one-dimensional CsCu_2I_3 nanowires for polarization-sensitive and flexible ultraviolet photodetectors," *Mater. Horiz.*, vol. 7, no. 6, pp. 1613–1622, 2020.
- [15] Q. Zhao et al., "High performance polarization-sensitive self-powered imaging photodetectors based on a p-Te/n- MoSe_2 van der Waals heterojunction with strong interlayer transition," *Mater. Horiz.*, vol. 8, no. 11, pp. 3113–3123, 2021.
- [16] H. Jiao et al., "HgCdTe/black phosphorus van der Waals heterojunction for high-performance polarization-sensitive midwave infrared photodetector," *Sci. Adv.*, vol. 8, no. 19, 2022, Art. no. eabn1811.
- [17] X. Yang et al., "Electronic and optical properties of a novel two-dimensional semiconductor material TiPt_2S_3 : A first-principles study," *Phys. Chem. Chem. Phys.*, vol. 24, no. 13, pp. 7642–7652, 2022.
- [18] W. Bronger and B. Bonsmann, "Ternäre Thalliumplatin- und Thalliumpalladiumchalkogenide $\text{Ti}_2\text{M}_4\text{X}_6$. Synthesen, kristallstruktur und bindungsverhältnisse," *Zeitschrift für Anorganische und Allgemeine Chemie*, vol. 621, no. 12, pp. 2083–2088, 1995.
- [19] V. Wang et al., "High-throughput computational screening of two-dimensional semiconductors," *J. Phys. Chem. Lett.*, vol. 13, no. 50, pp. 11581–11594, 2022.
- [20] J. Lahiri et al., "An extended defect in graphene as a metallic wire," *Nature Nanotechnol.*, vol. 5, no. 5, pp. 326–329, 2010.
- [21] Z.-H. Xu et al., "Effects of doping Ti, Nb, Ni on the photoelectric properties of monolayer 2H- WSe_2 ," *Physica E: Low-Dimensional Syst. Nanostruct.*, vol. 133, 2021, Art. no. 114846.
- [22] J. Jadowszczak et al., "MoS2 memtransistors fabricated by localized helium ion beam irradiation," *ACS Nano*, vol. 13, no. 12, pp. 14262–14273, 2019.
- [23] M. U. Rothmann et al., "Structural and chemical changes to $\text{CH}_3\text{NH}_3\text{PbI}_3$ induced by electron and gallium ion beams," *Adv. Mater.*, vol. 30, no. 25, 2018, Art. no. 1800629.
- [24] G. Kresse and J. Hafner, "Ab initio molecular dynamics for liquid metals," *Phys. Rev. B*, vol. 47, no. 1, pp. 558–561, 1993.
- [25] G. Kresse and J. Furthmüller, "Efficient iterative schemes for ab initio total-energy calculations using a plane-wave basis set," *Phys. Rev. B*, vol. 54, no. 16, pp. 11169–11186, 1996.
- [26] J. Taylor et al., "Ab initio modeling of quantum transport properties of molecular electronic devices," *Phys. Rev. B*, vol. 63, no. 24, 2001, Art. no. 245407.
- [27] Z. Xu et al., "Enhanced photogalvanic effects in the two-dimensional WTe_2 monolayer by vacancy- and substitution-doping," *Appl. Surf. Sci.*, vol. 548, 2021, Art. no. 148751.
- [28] S. Li et al., "Self-powered photogalvanic phosphorene photodetectors with high polarization sensitivity and suppressed dark current," *Nanoscale*, vol. 10, no. 16, pp. 7694–7701, 2018.
- [29] S. Gao et al., "Monolayer InSe photodetector with strong anisotropy and surface-bound excitons," *Phys. Chem. Chem. Phys.*, vol. 23, no. 10, pp. 6075–6083, 2021.
- [30] S. Li et al., "2D Perovskite $\text{Sr}_2\text{Nb}_3\text{O}_{10}$ for high-performance UV photodetectors," *Adv. Mater.*, vol. 32, no. 7, 2020, Art. no. 1905443.
- [31] C. Guo et al., "Anisotropic ultrasensitive PDTE₂-based phototransistor for room-temperature long-wavelength detection," *Sci. Adv.*, vol. 6, no. 36, 2020, Art. no. eabb6500.
- [32] J. Hu et al., "Optical response of Te-based monolayer materials from first principles," *Appl. Phys. Lett.*, vol. 115, no. 15, 2019, Art. no. 151104.
- [33] R. Graham et al., "Electric field dependent photocurrent decay length in single lead sulfide nanowire field effect transistors," *Nano Lett.*, vol. 11, no. 2, pp. 717–722, 2011.